

**Thermomagnetic properties of Bi<sub>2</sub>Te<sub>3</sub> single crystal in the temperature  
range from 55 K to 380 K**

Md Sabbir Akhanda<sup>a</sup>, S. Emad Rezaei<sup>a</sup>, Keivan Esfarjani<sup>b,c,d</sup>,  
Sergiy Krylyuk<sup>e</sup>, Albert V. Davydov<sup>e</sup>, Mona Zebarjadi<sup>a,b,\*</sup>

<sup>a</sup> *Department of Electrical and Computer Engineering, University of Virginia, Charlottesville, Virginia 22904, USA*

<sup>b</sup> *Department of Materials Science and Engineering, University of Virginia, Charlottesville, Virginia 22904, USA*

<sup>c</sup> *Department of Mechanical and Aerospace Engineering, University of Virginia, Charlottesville, Virginia 22904, USA*

<sup>d</sup> *Department of Physics, University of Virginia, Charlottesville, Virginia 22904, USA*

<sup>e</sup> *Material Science and Engineering Division, National Institute of Standards and Technology, Gaithersburg, MD 20899, USA*

\* E-mail address: [m.zebarjadi@virginia.edu](mailto:m.zebarjadi@virginia.edu)

## Abstract

Magneto-thermoelectric transport provides an understanding of coupled electron-hole-phonon current in topological materials and has applications in energy conversion and cooling. In this work, we study the Nernst coefficient, the magneto-Seebeck coefficient, and the magnetoresistance of single-crystalline Bi<sub>2</sub>Te<sub>3</sub> under external magnetic field in the range of -3 T to 3 T and in the temperature range of 55 K to 380 K. Moreau's relation is employed to justify both the overall trend of the Nernst coefficient and the temperature at which the Nernst coefficient changes sign. We observe a non-linear relationship between the Nernst coefficient and the applied magnetic field in the temperature range of 55 K to 255 K. An increase in both the Nernst coefficient and the magneto-Seebeck coefficient is observed as the temperature is reduced which can be attributed to the increased mobility of the carriers at lower temperatures. First-principles density functional theory calculations were carried out to physically model the experimental data including electronic and transport properties. Simulation findings agreed with the experiments and provide a theoretical insight to justify the measurements.

## I. Introduction

The first observation of cooling using a Bi<sub>2</sub>Te<sub>3</sub> thermocouple about seventy-five years ago inspired a surge of interest in the field of thermoelectric energy conversion [1]. Identifying suitable new materials and enhancing the thermoelectric properties of the already recognized ones have been the major research drive of the thermoelectric research community since then [2–19]. The thermoelectric performance of a material is evaluated by its dimensionless figure of merit,  $z_{TE}T$ , defined as  $\sigma^2ST/\kappa$  where  $\sigma$  is the electrical conductivity,  $S$  is the Seebeck coefficient,  $\kappa$  is the thermal conductivity, and  $T$  is the average temperature of the material. Despite the discovery of numerous other

thermoelectric materials to this date,  $\text{Bi}_2\text{Te}_3$  and its alloys (with  $\text{Sb}_2\text{Te}_3$  for p-type and with  $\text{Bi}_2\text{Se}_3$  for n-type conductivity, respectively) are still the dominant materials used in commercial thermoelectric modules for near room-temperature applications. [20] Hence, it is no surprise that a large number of articles are focused on the study of  $\text{Bi}_2\text{Te}_3$  thermoelectric transport properties [21–25]. Bismuth Sesquitelluride  $\text{Bi}_2\text{Te}_3$  is a layered material and inherently has low thermal conductivity [26]. At the same time, it is a topological material with a complex band structure [27]. Many detailed first-principles studies have been reported so far to better understand the electronic band structure and consequently thermoelectric properties of the  $\text{Bi}_2\text{Te}_3$  family [27–35]. Due to spin-orbit interaction,  $\text{Bi}_2\text{Te}_3$  has band inversion with band extrema that are not at the high symmetry  $\Gamma$  point [27]. The resulted valleys have small effective masses and high valley degeneracy, making the electronic band structure of Bismuth Sesquitelluride  $\text{Bi}_2\text{Te}_3$  ideal for thermoelectric applications. Various reports on the Seebeck coefficient and the Hall measurement of extrinsic samples pointed to the necessity of a six-valley band model to properly describe the relationship between the Hall coefficient and the carrier concentration [36–39]. While examining the thermal conductivity behavior at a temperature range of 77 K to 380 K, Satterthwaite and Ure reported a sharp rise in the thermal conductivity around room temperature and above due to ambipolar diffusion of electrons and holes. [26] Goldsmid found that the lattice thermal conductivity of doped  $\text{Bi}_2\text{Te}_3$  is independent of its electrical conductivity [40]. He reported that doping with

halogen atoms is an exception and results in the reduction of lattice thermal conductivity due to the large cross-section of phonon-halogen atom scattering.

While the thermoelectric properties of  $\text{Bi}_2\text{Te}_3$  have been well-studied to attain a higher figure of merit, the thermomagnetic properties lack the same research depth. When a magnetic field is applied in the  $z$ -direction, i.e., normal to the basal (0001) crystal plane in  $\text{Bi}_2\text{Te}_3$ , the thermomagnetic figure of merit,  $z_{TM}T$  is defined as  $(N^2\sigma_{yy}T)/\kappa_{xx}$  where  $N$  is the Nernst coefficient in the unit of  $\mu\text{V}/\text{K}$ ,  $\sigma_{yy}$  is the electrical conductivity in the  $y$ -direction,  $\kappa_{xx}$  is the thermal conductivity along the direction of the applied thermal gradient, and  $T$  is the average temperature of the material [41]. The Nernst coefficient in the thermomagnetic transport is the transverse equivalent of the Seebeck coefficient  $S_{xx}$  in the thermoelectric transport. Thermomagnetic power generators and coolers are an alternative to thermoelectric modules. They have several advantages compared to their thermoelectric counterparts such as exhibiting higher energy conversion efficiency for the same  $zT$  (adiabatic) (applicable when the  $zT$  (adiabatic) is roughly greater than 0.2) [42,43], better suitability for energy conversion in the case of thin films, and simpler design as the module can be made using only one material compared to two (n-type and p-type) in case of a thermoelectric module [43,44]. The potential that the transverse thermomagnetic properties hold in energy conversion can duly be stressed by taking the Dirac semimetal  $\text{Cd}_3\text{As}_2$  as an example. In a recently published paper, it has been reported that  $\text{Cd}_3\text{As}_2$  has a transverse thermomagnetic  $z_{TM}T \approx 0.5$  at room temperature which is

more than twice its longitudinal thermoelectric  $z_{TE}T$  [45]. The study of the Nernst effect is also important in spintronics. It has recently been shown that the Nernst voltage can be a source of spurious signal in spin-orbit torque measurements in topological insulators [46]. The magnetization dynamics can be controlled by thermally driven spin Nernst torque [47]. Therefore, taking a closer look at the thermomagnetic properties of  $\text{Bi}_2\text{Te}_3$  is evidently fitting. To our best knowledge, only a few attempts have been made to study the Nernst effect in  $\text{Bi}_2\text{Te}_3$  so far. Mansfield and Williams in 1958 measured the Nernst coefficient of  $\text{Bi}_2\text{Te}_3$  under a magnetic field of 1.4 T and reported a slow increase in the coefficient with decreasing temperature [48]. In 1966, Champness and Kipling measured the Nernst coefficient for an n-type  $\text{Bi}_2\text{Te}_3$  under a constant magnetic field of 1.88 T applied parallel to the cleavage plane and concluded that the electron to hole mobility ratio decreases up to room temperature [49]. In 1997, Zhitinskaya et al. used their Nernst measurement at 300 K in the weak magnetic field regime as a means to predict the degree of inhomogeneity present in the  $\text{Bi}_2\text{Te}_3$  crystal [50]. All these studies revealed useful information but do not provide a complete picture of the Nernst effect covering both large magnetic fields and a wide temperature range.

In this work, we report the measurement of the Nernst coefficient of  $\text{Bi}_2\text{Te}_3$  over a wide range of magnetic fields and temperatures. We observed a change in the sign of the Nernst coefficient as predicted by the Moreau's relation [51] [Eq. (1)] around the same temperature at which the Seebeck coefficient peaks. We also observed a non-linear

behavior of the Nernst coefficient versus  $H$  in the high magnetic field regime ( $\mu H > 1$ ). The measurement of thermoelectric properties, Hall coefficient, magneto-Seebeck, and magnetoresistance were included in this report to provide a more complete perspective. We used first-principles calculations and analytical solutions of the Boltzmann transport equation (BTE) using the constant relaxation time approximation and in the presence of an externally applied magnetic field are used to calculate magnetotransport responses. In the absence of the magnetic field, theoretical Seebeck coefficients accurately reproduce the experimental ones. The presence of the magnetic field introduces the magneto-Seebeck, the magnetoresistance, and the Nernst signal. Finally, the Nernst signal was calculated using phenomenological models. The trends seen in the theoretical result agrees with that of the experiment, but these are not in quantitative agreement primarily due to the use of constant relaxation time approximation (CRTA) during the theoretical calculations.

$$N = TR_H\sigma \frac{\partial S}{\partial T} \quad (1)$$

## II. Materials and Methods

### *A. Experimental details*

An undoped  $\text{Bi}_2\text{Te}_3$  was grown by the vertical Bridgman method. Polycrystalline  $\text{Bi}_2\text{Te}_3$  powder ( $\approx 15$  g) was loaded in a graphitized quartz ampoule (10 mm inner diameter) that was sealed under vacuum and placed in a single-zone furnace. After homogenization of

the melt at 630 °C for several hours, the ampoule was transferred through a temperature gradient of  $\approx 50$  °C/cm at a speed of 0.5 mm/h. The growth run produced a single-crystalline Bi<sub>2</sub>Te<sub>3</sub> ingot with the cleavage plane parallel to the ampoule axis. The sample (8.7 × 3.9 × 1.5 mm<sup>3</sup> (L × W × H)) was cut from the central part of the ingot. Gold-plated flat copper wire of 0.5 mm width was used to make contact electrodes. A two-component silver-filled epoxy was used to glue the contact wires to the sample. The thermoelectric properties of the sample, at a temperature range 55 K to 380 K and magnetic field of -3 T to 3 T, were measured by the one-heater and two-thermometer configuration using the thermal transport option (TTO) of the VersaLab (Quantum design Inc.). The applied magnetic field was perpendicular to the direction of the thermal gradient and the cleavage plane. To establish a thermal gradient along the length of the sample, a resistive heater was attached to one end of the sample. Another contact attached at the opposite end of the sample was clamped to the cold foot of the TTO puck which acted as a heatsink. Thus, the temperature difference is applied between two parallel heat sink and heat source placed 8.7 mm apart, implying that the slow transverse voltage measurements are done under nearly isothermal conditions, and the reported Nernst coefficients are the isothermal values rather than the smaller adiabatic values. Two TTO shoes placed 3.4 mm apart were employed to measure the temperature and the voltage difference simultaneously. For the Seebeck measurement over the entire range of temperature, an adaptive measurement mode was used that maintained the temperature difference

within (1 to 3) % of the sample temperature. Taking into account the geometrical factor of the sample and Versalab system specification, the estimated errors in the Seebeck, thermal conductivity, and resistivity measurement were about 5 %, 10 %, and 3 % respectively. Nernst measurement was also carried out using the one-heater two-thermometer configuration in the temperature range of 55 K to 300 K. Magnetic field with a step increase of 1 T was applied up to 3 T in both z and -z directions. Transverse voltage was measured by two voltage probes attached to two gold-coated copper contacts placed perpendicular to the thermal gradient and the magnetic field directions. The estimated error in the Nernst measurement was  $\approx 10\%$  (the main error sources include fitting errors of VERSALAB software, error in measurement of the sample size, nonuniformity of the temperature gradient, and instrumental errors). To determine the carrier concentration, a four-probe Hall measurement was carried out using the electrical transport option (ETO) of VersaLab in the temperature range of 50 K to 380 K. In this measurement, two voltage leads were placed transversely to the direction in which the current and the magnetic field were applied. The estimated error in the measurement was  $\approx 5\%$ . The thermal gradient and magnetic field applied in all measurements described above were parallel and perpendicular to the material's cleavage plane, respectively.

## *B. Computational details*

The QUANTUM-ESPRESSO software package [52] was employed to carry out first-principles density functional theory (DFT) calculations with ultra-soft pseudopotentials [53] and with the Perdew–Burke–Ernzerhof exchange-correlation functional [54]. An  $8 \times 8 \times 8$  Monkhorst–Pack k-point mesh was chosen to reproduce electronic states in the first Brillouin zone and kinetic energy cutoffs for charge density and wave function were set to be 700 Ry and 70 Ry, respectively. Experimental lattice constants of  $a=10.473 \text{ \AA}$  and  $\theta_{\text{Bi-Te}}=24.17^\circ$  [33] were utilized to simulate the structure. Atomic positions were relaxed to minimize energy. Transport properties were assessed through the semiclassical Boltzmann theory as implemented in the BoltzTraP package [55]. Modifications under the magnetic field will be discussed in the results.

## **III. Results and Discussion**

The Spin-orbit coupling (SOC) effect plays an important role in the electronic structure calculations. [56] Figure 1 (a) compares the band structure of  $\text{Bi}_2\text{Te}_3$  with and without SOC. The inclusion of SOC results in a significant reduction in the bandgap from 0.29 eV to 0.11 eV and a significant change in the effective mass values. For example, at  $\Gamma$  point, the conduction band effective mass increases from  $0.15m_0$  to  $0.7m_0$  after introducing SOC effects. Finally, band inversion happens at  $\Gamma$  point in the presence of the SOC effect. Our

results are in agreement with previous calculations [57] and the obtained bandgap of 0.11 eV is close to the experimentally measured bandgap of 0.15 eV [58].

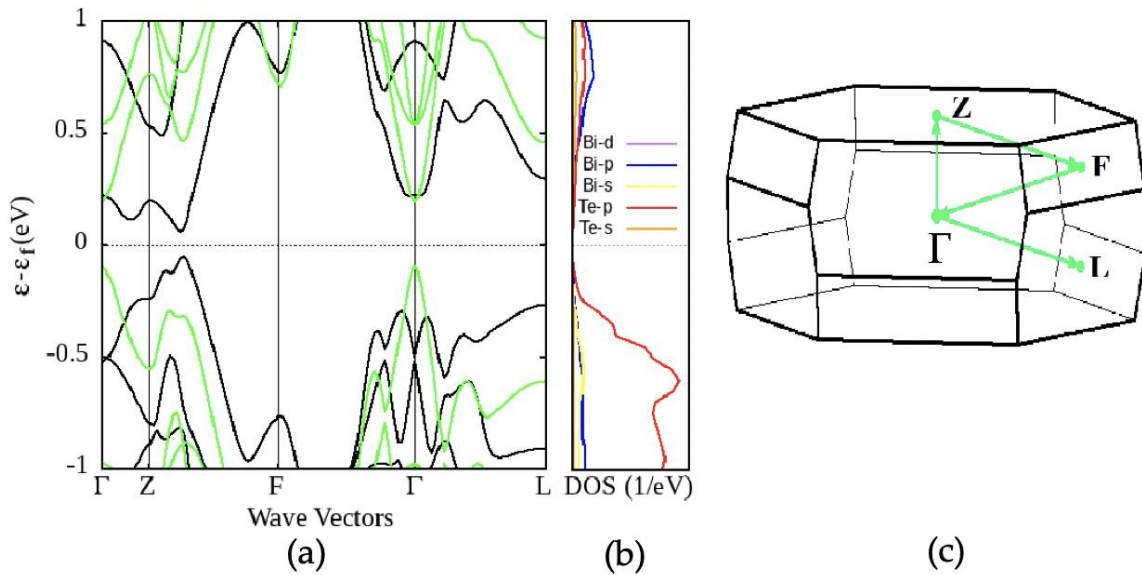


Figure 1. a) Band structure of  $\text{Bi}_2\text{Te}_3$  with (black) and without (green) SOC effect. The presence of SOC lowers the bandgap and  $\text{Bi}_2\text{Te}_3$  turns to a narrow-gap semiconductor. b) The projected density of states (DOS) including SOC shows that valence and conduction bands are mainly formed by Te and Bi p-orbitals, respectively. c) Brillouin zone for  $\text{Bi}_2\text{Te}_3$  crystal structure.

The contribution of each atomic orbital to the total density of states is shown in the right panel of Figure 1 (b). The valence band is dominated by p-orbitals of tellurium and the conduction band is mostly composed of p-orbitals of bismuth, which is in agreement with the projected band structure (Figure 2). Color bar in Figure 2 indicates contribution of a specific orbital in each band from the lowest (green) to the highest (yellow) contribution [e.g., in Figure 2 (a) valence band is more blue-red which shows a high contribution of p-

orbitals of Bi]. In this figure band inversion of the Bi-p orbitals can be seen: the valence band acquires a Bi-p component near the  $\Gamma$  point.

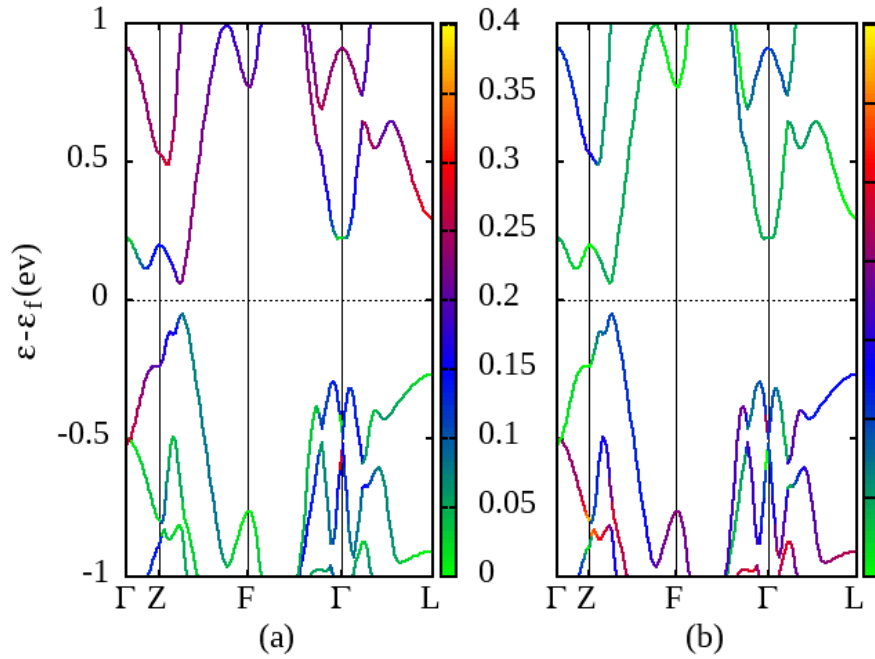


Figure 2. Contribution of p-orbitals of (a) Bi and (b) Te. Similar to projected DOS, p-orbitals of Bi and Te form valence and conduction bands. The color bar was kept identical for all projection. The valence band of Bi<sub>2</sub>Te<sub>3</sub> is mostly of type Te-p (right figure) and the conduction band is mostly of type Bi-p (left figure)

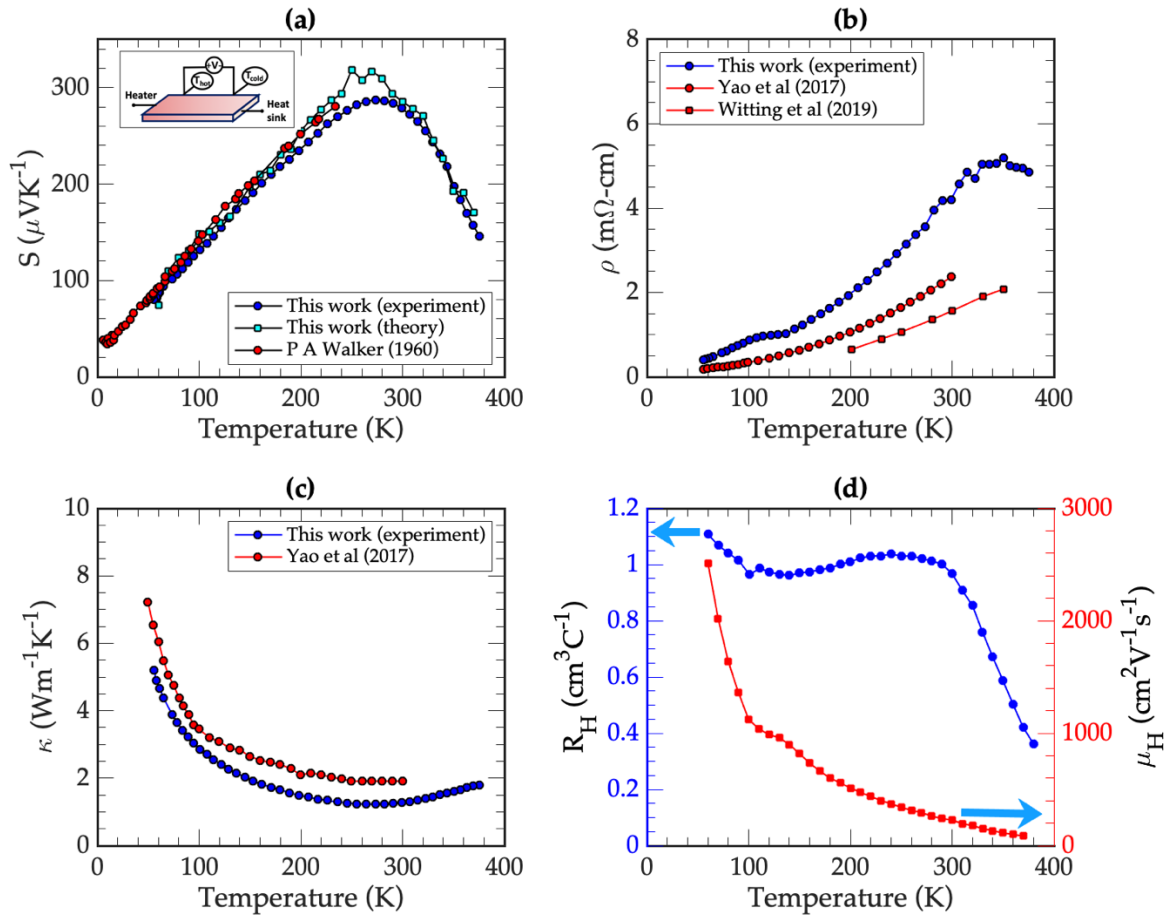


Figure 3. Variation of electrical and thermal properties of single-crystal  $\text{Bi}_2\text{Te}_3$  with temperature: (a) Seebeck coefficient, (b) resistivity, (c) thermal conductivity, and (d) Hall coefficient  $R_H$  and Hall mobility  $\mu_H$ .

The temperature dependence of the transport coefficients including the Seebeck coefficient,  $S$ , the electrical and thermal conductivity, the Hall coefficient, and the carrier mobility is shown in Figure 3. Our measured sample has mobility of  $227 \text{ cm}^2\text{V}^{-1}\text{s}^{-1}$  at 300 K which is very close to the ones reported by other sources on similar samples [26,38,59]. Carrier concentrations were computed from experimental Hall coefficient values, for which the corresponding chemical potentials were estimated through the first-principles calculations followed by Seebeck coefficient computation of

each chemical potential. Experimentally measured Seebeck values were reproduced by first-principles calculations (explained in the computational detail sub-section). It is noteworthy to say that small deviations between theory and experiments could come from constant relaxation time approximation assumption.

The Seebeck coefficient trend over the entire temperature range can be divided into two distinct regions as also noted by many previous reports on  $\text{Bi}_2\text{Te}_3$  [22,36,60]. The separation is roughly at 273 K where the Seebeck coefficient reaches its peak value of +287  $\mu\text{V}/\text{K}$ . Below 273 K, the carrier concentration does not change significantly as evidenced by a weak change of the Hall coefficient (Figure 3 (d)). In this range, as temperature increases, the carrier mobility decreases due to the increase in the electron-phonon scattering rates. Hence, we observe a metallic behavior where resistivity increases with temperature. In this regime, since the free carrier density is almost fixed, as we increase the temperature, the quasi-Fermi level moves closer to the middle of the gap increasing the Seebeck coefficient. Beyond 273 K, intrinsic carriers excited across the bandgap dominate conductivity. In this region, we see a decrease in the Seebeck coefficient with increasing temperature as both electrons and holes are generated (the bipolar effect). The resistivity starts to decrease due to the increase in carrier concentration. The sign of the Seebeck coefficient remains positive throughout the entire temperature range which is a confirmation that the sample is nominally p-type doped.  $\text{Bi}_2\text{Te}_3$  is known as a topological insulator [27]. However, the  $\text{Bi}_2\text{Te}_3$  single crystal is naturally p-type and its bulk energy

bands are characterized by a small band gap and are strongly influenced by spin-orbit interactions. Hence, it is difficult to observe an electrically insulating bulk [61]. In particular, in the temperature range of our study, the sample behaves as a metal rather than an insulator. We also note that even though our calculations only included the bulk states, they can describe the Seebeck coefficient in agreement with the experiment [as shown in Fig. 3(a)]. We expect the surface states are dominant at much lower temperatures [62] and much lower thicknesses [63]. In semiconductors, total thermal conductivity has contributions from phonons, electrons, and bipolar transport [64]. In the temperature range of 55 K to 200 K, thermal transport is dominated by phonon thermal conductivity. As we increase the temperature, we see a decreasing trend in the thermal conductivity due to the increase in anharmonic phonon scattering as shown in Figure 3 (c). At higher temperatures (above 300 K), the bipolar contribution becomes significant and results in a rise in the total thermal conductivity. Figure 3(d) shows the measured Hall coefficient and the extracted carrier Hall mobility. We need to point out that at temperatures above 273 K, where bipolar conduction starts, the extracted Hall mobility is very different from the drift mobility and we cannot separately extract the drift mobility of electrons and holes. The Hall coefficient is proportional to the inverse of the difference between the number of holes and electrons, while the electrical conductivity is the sum of the electron conductivity and hole

conductivity. The Hall mobility is extracted by dividing the electrical conductivity by the Hall carrier concentration.

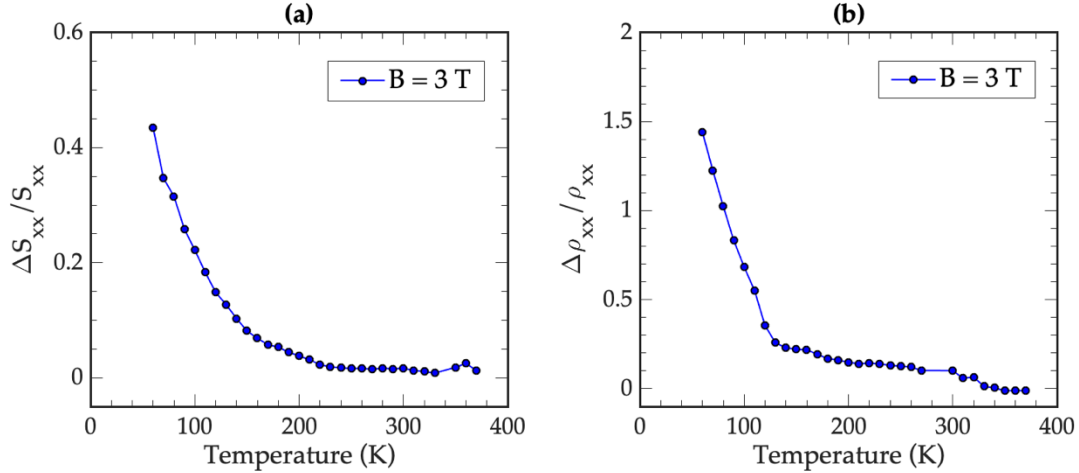


Figure 4 Plot of the temperature dependence of (a) magneto-Seebeck and (b) magneto-resistance. Here,  $S_{xx}$  and  $\rho_{xx}$  are the Seebeck coefficient and resistivity measured along the length of the sample under zero magnetic field and  $\Delta S_{xx}$  and  $\Delta \rho_{xx}$  are the respective change in these quantities once a magnetic field is applied

Figure 4 shows the temperature dependence of the magneto-Seebeck and the magneto-resistance of the sample in the magnetic field range of 1 T to 3 T applied perpendicular to both the thermal gradient and the cleavage plane. Each data points were obtained by applying the magnetic field both in positive and negative directions and then averaging the corresponding  $\Delta S_{xx}$  and  $\Delta \rho_{xx}$  responses. The change in the Seebeck coefficient and resistivity are always positive below 375 K. The decrease in the value of the magneto-Seebeck and magneto-resistance versus temperature can be attributed to the reduced mobility at higher temperatures.

Figure 5(a) shows the sample mounted on a TTO puck for the Nernst measurement. Temperature dependence of the Nernst coefficient is shown in Fig. 5(b) and temperature dependence of the thermoelectric and thermomagnetic  $zT$  has been included in the

Supplemental Material [65]. Here also, for each data points, the magnetic field was applied both in positive and negative directions and the responses were averaged. The Nernst signal, similar to the magneto-Seebeck and magnetoresistance, increases as we decrease the temperature. In the same graph, we also plotted the Nernst coefficient of this material calculated using the Moreau's relation [51]. According to this relation, the Nernst coefficient of a material can be written as the negative of the product of its Thompson coefficient (defined as the product of the temperature of the sample and the first derivative of its Seebeck coefficient with respect to the temperature) [51], Hall coefficient, and electrical conductivity. Moreau's relation predicts a change in the sign and a zero Nernst signal at the same temperature at which the Seebeck coefficient peaks ( $\approx 273$  K for this sample). Our experimental data show that the Nernst signal changed its sign at about 255 K which is in close agreement with Moreau's prediction. The difference stems from the inaccuracy of the Moreau's relation as well as error bar in the measurements of the involved transport coefficients (the Seebeck coefficient, Hall coefficient, the electrical conductivity, and the Nernst coefficient). We note that Moreau's relation is only accurate for metals. However, as shown, it can still closely replicate the results of  $\text{Bi}_2\text{Te}_3$ , a narrow-gap semiconductor. Above 255 K, the Nernst coefficient is positive and maintains a linear relationship with the applied magnetic field. But below 255 K, the linearity ceases quickly and non-linear behavior of the Nernst coefficient versus the magnetic field slowly emerges (Figure 5d). This non-linear behavior intensifies as we go down in temperature.

Moreau's relation cannot account for this non-linearity. The basis of this behavior becomes apparent when the Boltzmann Transport Equation under a magnetic field is solved. The following formalism is developed after Behnia [66] and following Smith's [67] notation. Electrical current density under an external magnetic field (H) can be written as:

$$\begin{bmatrix} J_x \\ J_y \end{bmatrix} = \begin{bmatrix} \sigma(H)_{xx} & \sigma(H)_{xy} \\ \sigma(H)_{yx} & \sigma(H)_{yy} \end{bmatrix} \begin{bmatrix} E_x \\ E_y \end{bmatrix} + \begin{bmatrix} B(H)_{xx} & B(H)_{xy} \\ B(H)_{yx} & B(H)_{yy} \end{bmatrix} \begin{bmatrix} -\frac{\partial_x T}{T^2} \\ -\frac{\partial_y T}{T^2} \end{bmatrix} \quad (2)$$

Assuming there is no temperature gradient along the y-direction (isothermal condition for the Nernst coefficient), Eq.2 can be simplified as follows:

$$J_x = \sigma_{xx}(H)E_x + \sigma_{xy}(H)E_y - \frac{B_{xx}(H)}{T^2} \nabla_x T, \quad (3)$$

$$J_y = \sigma_{yx}(H)E_x + \sigma_{yy}(H)E_y - \frac{B_{yx}(H)}{T^2} \nabla_x T, \quad (4)$$

where  $\sigma(H)$  and  $B(H)$  are the response function tensors defined as:

$$\sigma_{ij} = q^2 \int \tau v_i v_j \left( -\frac{\partial f_0^k}{\partial E} \right) \frac{d^3 k}{4\pi^3}, \quad (5)$$

$$[B] = \frac{q}{T} \int (E_k - \mu) \frac{\partial f_0^k}{\partial E} \frac{\tau}{(1+\mu H)^2} \begin{bmatrix} v_x^2 & v_x v_y - v_x^2 \mu H & v_z v_x \\ v_x v_y + v_y^2 \mu H & v_y^2 & v_z v_y \\ v_z v_x & v_z v_y & v_z^2 (1 + \mu^2 H^2) \end{bmatrix} \frac{d^3 k}{4\pi^3} \quad (6)$$

The Nernst coefficient is defined under open-circuit conditions when the electrical current is zero in all directions and the magnetic field is applied only along the z-axis. In

these circumstances, eliminating  $E_x$  using Eqs. (3) and (4), and using the definition of the isothermal Nernst coefficient, we find:

$$N_{xyz} = E_y / \partial_x T = \frac{1}{T^2} \frac{\sigma_{xx} B_{yx} - \sigma_{yx} B_{xx}}{\sigma_{xx} \sigma_{yy} - \sigma_{yx} \sigma_{xy}} \quad (7)$$

To calculate the Nernst coefficient, we used the band structure and the differential conductivity calculated using first-principles calculations as described in the computational details section. The experimental mobility was used in Eq. (5). The Nernst coefficient computed from Eq. (6) is plotted in Figure 5(c) and compared with the experimental data. The current calculation is performed under constant relaxation time approximation, assuming that the relaxation times do not change under an externally applied magnetic field. However, Smith *et al.* [65] have shown that the changes in the relaxation times versus the magnetic field add another term in the Nernst coefficient. Hence, we believe that the main discrepancy between the theory and experiment is the constant relaxation time approximation used in the theory. Finally, we note that Fig. 5(c) confirms that an increase in the Nernst coefficient at lower carrier concentrations, lower temperatures, and larger magnetic fields as reported in other materials [68] is also valid for this material. The non-linearity vs magnetic field, as can be seen in Figure 5c, is strongest at the lowest measured temperature, 55 K, pointing to the suitability of the Nernst effect in cryogenic energy conversion application.

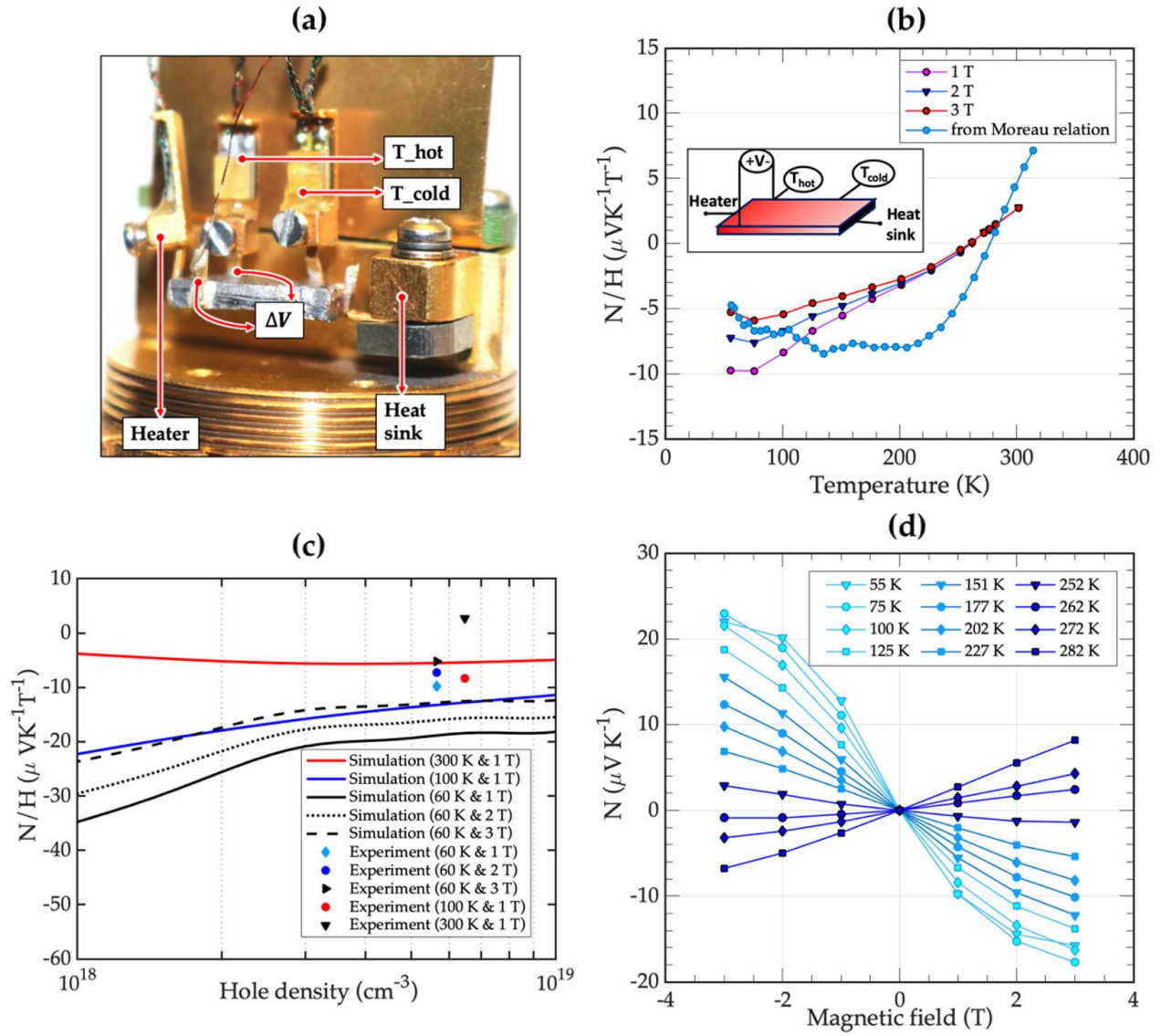


Figure 5. (a) Mounted sample on the TTO puck. (b) Temperature dependence of Nernst coefficient ( $N/H$ ) obtained from experiment and Moreau's relation. (c) Nernst coefficient ( $N/H$ ) at different hole concentration calculated using Eqs. (5) and (6) with inputs from first-principles calculations. (d) Magnetic field dependence of the Nernst coefficient ( $N$ ).

#### IV Conclusion:

In summary, we studied the Nernst coefficient, magneto-Seebeck, and magnetoresistance of single-crystal  $\text{Bi}_2\text{Te}_3$  under the effect of an external magnetic field ( $<3$  T) and temperature (55 K to 380 K). The Nernst coefficient changes its sign at about 255 K as

predicted by the Moreau's relation. It shows a nonlinear trend versus the applied magnetic field at low temperatures. The nonlinearity gradually increases as the temperature decreases. The magnitudes of the magneto-Seebeck and magnetoresistance were also found to increase as the temperature was decreased. First-principles calculations along with constant relaxation time approximation (CTRA) were used within the framework of BOLTZTRAP to calculate the Seebeck coefficient and it is in close agreement with the experimentally measured values. The formalism developed by Behnia and Smith was used to calculate the Nernst coefficient of the sample. The theoretical calculations can successfully explain the trends observed in the experiment but are not in quantitative agreement. The discrepancy is attributed to the use of CRTA. Our experimental data and theoretical calculation confirm that the material under study shows the general trend of exhibiting higher values of the Nernst and magneto-Seebeck coefficients at higher mobility values. Our theoretical results show that the magnitude of the Nernst coefficient is larger at lower temperatures, lower carrier concentrations, and larger magnetic fields. These observations could prove useful in evaluating the Nernst coefficient in other materials having similar band structures as that of  $\text{Bi}_2\text{Te}_3$ .

## ACKNOWLEDGMENTS

The work at UVA is supported by DOE-SC Grant No. DE-SC0019552. We acknowledge the Rivanna cluster of UVA for providing the computational resources. S.K. and A.V.D. acknowledge support from Material Genome Initiative funding allocated to NIST.

## Disclaimer

Certain commercial equipment, instruments, or materials are identified in this paper in order to specify the experimental procedure adequately. Such identification is not intended to imply recommendation or endorsement by the National Institute of Standards and Technology, nor is it intended to imply that the materials or equipment identified are necessarily the best available for the purpose.

## References:

- [1] H. J. Goldsmid and R. W. Douglas, The use of semiconductors in thermoelectric refrigeration, *Br. J. Appl. Phys.* 5, 386 (1954).
- [2] G. J. Snyder and E. S. Toberer, Complex thermoelectric materials, in *Materials for Sustainable Energy: A Collection of Peer-Reviewed Research and Review Articles from Nature Publishing Group* (World Scientific Publishing, Singapore, 2010), pp. 101–110.
- [3] G. D. Mahan and J. O. Sofo, The best thermoelectric, *Proc. Nat. Acad. Sci. USA* 93, 7436 (1996).
- [4] F. J. DiSalvo, Thermoelectric cooling and power generation, *Science* 285, 703 (1999).
- [5] Y. I. Ravich and D. A. Pshenai-Severin, Thermoelectric figure of merit of a p-n junction, *Semiconductors* 35, 1161 (2001).
- [6] A. I. Hochbaum, R. Chen, R. D. Delgado, W. Liang, E. C. Garnett, M. Najarian, A. Majumdar, and P. Yang, Enhanced thermoelectric performance of rough silicon nanowires, *Nature (London)* 451, 163 (2008).
- [7] A. I. Boukai, Y. Bunimovich, J. Tahir-Kheli, J. K. Yu, W. A. Goddard, and J. R. Heath, Silicon nanowires as efficient thermoelectric materials, *Nature (London)* 451, 168 (2008).
- [8] T. C. Harman, P. J. Taylor, M. P. Walsh, and B. E. LaForge, Quantum dot superlattice thermoelectric materials and devices, *Science* 297, 2229 (2002).
- [9] J. F. Li, W. S. Liu, L. D. Zhao, and M. Zhou, High-performance nanostructured thermoelectric materials *NPG Asia Materials* 2, 152 (2010).
- [10] C. Wood, Materials for thermoelectric energy conversion, *Rep. Prog. Phys.* 51, 459 (1988).
- [11] G. Chen, M. S. Dresselhaus, G. Dresselhaus, J. P. Fleurial, and T. Caillat, Recent developments in thermoelectric materials, *Int. Mater. Rev.* 48, 45 (2003).
- [12] S. Volz (Ed.), in *Thermal Nanosystems and Nanomaterials*, 1st ed., *Topics in Applied Physics* Vol. 118 (Springer-Verlag, Berlin, Heidelberg, 2009).
- [13] G. S. Nolas, J. L. Cohn, G. A. Slack, and S. B. Schujman, Semiconducting Ge clathrates:

Promising candidates for thermoelectric applications, *Appl. Phys. Lett.* 73, 178 (1998).

[14] M. S. Dresselhaus, G. Dresselhaus, X. Sun, Z. Zhang, S. B. Cronin, and T. Koga, Low-dimensional thermoelectric materials, in *Physics of the Solid State* (American Institute of Physics, College Park, MD, 1999), Vol. 41, pp. 679–682.

[15] M. Zebarjadi, G. Joshi, G. Zhu, B. Yu, A. Minnich, Y. Lan, X. Wang, M. Dresselhaus, Z. Ren, and G. Chen, Power factor enhancement by modulation doping in bulk nanocomposites, *Nano Lett.* 11, 2225 (2011).

[16] B. Yu, M. Zebarjadi, H. Wang, K. Lukas, H. Wang, D. Wang, C. Opeil, M. Dresselhaus, G. Chen, and Z. Ren, Enhancement of thermoelectric properties by modulation-doping in silicon germanium alloy nanocomposites, *Nano Lett.* 12, 2077 (2012).

[17] M. Zebarjadi, B. Liao, K. Esfarjani, M. Dresselhaus, and G. Chen, Enhancing the thermoelectric power factor by using invisible dopants, *Adv. Mater.* 25, 1577 (2013).

[18] M. Markov, X. Hu, H. C. Liu, N. Liu, S. J. Poon, K. Esfarjani, and M. Zebarjadi, Semimetals as potential thermoelectric materials, *Sci. Rep.* 8, 9876 (2018).

[19] N. Liu, S. E. Rezaei, W. A. Jensen, S. Song, Z. Ren, K. Esfarjani, M. Zebarjadi, and J. A. Floro, Improved thermoelectric performance of eco-friendly  $\beta$ -FeSi<sub>2</sub>-SiGe nanocomposite via synergistic hierarchical structuring, phase percolation, and selective doping, *Adv. Funct. Mater.* 29, 1903157 (2019).

[20] Z. Soleimani, S. Zoras, B. Ceranic, S. Shahzad, and Y. Cui, A review on recent for room-temperature applications, *Sustain. Energy Technol. Assess.* 37, 100604 (2020).

[21] M. Yao, C. Opeil, S. Wilson, and M. Zebarjadi, Experimental determination of phonon thermal conductivity and Lorenz ratio of single-crystal bismuth telluride, *MRS Commun.* 7, 922 (2017).

[22] I. T. Witting, T. C. Chasapis, F. Ricci, M. Peters, N. A. Heinz, G. Hautier, and G. J. Snyder, The thermoelectric properties of bismuth telluride, *Adv. Electron. Mater.* 5, 1800904 (2019).

[23] P. Graziosi, C. Kumarasinghe, and N. Neophytou, Impact of the scattering physics on the power factor of complex thermoelectric materials, *J. Appl. Phys.* 126, 155701 (2019).

[24] M. Markov, S. E. Rezaei, S. N. Sadeghi, K. Esfarjani, and M. Zebarjadi, Thermoelectric properties of semimetals, *Phys. Rev. Mater.* 3, 095401 (2019).

[25] D. X. Qu, Y. S. Hor, J. Xiong, R. J. Cava, and N. P. Ong, Quantum oscillations and hall anomaly of surface states in the topological insulator Bi<sub>2</sub>Te<sub>3</sub>, *Science* 329, 821 (2010).

[26] C. B. Satterthwaite and R. W. Ure, Electrical and thermal properties of Bi<sub>2</sub>Te<sub>3</sub>, *Phys. Rev.* 108, 1164 (1957).

[27] H. Zhang, C. X. Liu, X. L. Qi, X. Dai, Z. Fang, and S. C. Zhang, Topological insulators in Bi<sub>2</sub>Se<sub>3</sub>, Bi<sub>2</sub>Te<sub>3</sub> and Sb<sub>2</sub>Te<sub>3</sub> with a single Dirac cone on the surface, *Nat. Phys.* 5, 438 (2009).

- [28] P. Larson, S. D. Mahanti, and M. G. Kanatzidis, Electronic structure and transport of Bi<sub>2</sub>Te<sub>3</sub> and BaBiTe<sub>3</sub>, *Phys. Rev. B* 61, 8162 (2000).
- [29] S. J. Youn and A. J. Freeman, First-principles electronic structure and its relation to thermoelectric properties of Bi<sub>2</sub>Te<sub>3</sub>, *Phys. Rev. B* 63, 085112 (2001).
- [30] T. J. Scheidemantel, C. Ambrosch-Draxl, T. Thonhauser, J. V. Badding, and J. O. Sofo, Transport coefficients from firstprinciples calculations, *Phys. Rev. B* 68, 125210 (2003).
- [31] M. Kim, A. J. Freeman, and C. B. Geller, Screened exchange LDA determination of the ground and excited state properties of thermoelectrics: Bi<sub>2</sub>Te<sub>3</sub>, *Phys. Rev. B* 72, 035205 (2005).
- [32] B.-L. Huang and M. Kaviani, Ab initio and molecular dynamics predictions for electron and phonon transport in bismuth telluride, *Phys. Rev. B* 77, 125209 (2008).
- [33] B. Y. Yavorsky, N. F. Hinsche, I. Mertig, and P. Zahn, Electronic structure and transport anisotropy of Bi<sub>2</sub>Te<sub>3</sub> and Sb<sub>2</sub>Te<sub>3</sub>, *Phys. Rev. B* 84, 165208 (2011).
- [34] B. Ryu and M.-W. Oh, Computational simulations of thermoelectric transport properties, *J. Korean Ceram. Soc.* 53, 273 (2016).
- [35] T. Fang, X. Li, C. Hu, Q. Zhang, J. Yang, W. Zhang, X. Zhao, D. Singh, and T. Zhu, Complex band structures and lattice dynamics of Bi<sub>2</sub>Te<sub>3</sub>-based compounds and solid solutions, *Adv. Funct. Mater.* 29, 1900677 (2019).
- [36] H. J. Goldsmid, The electrical conductivity and thermoelectric power of bismuth telluride, *Proc. Phys. Soc.* 71, 633 (1958).
- [37] J. R. Drabble, R. D. Groves, and R. Wolfe, Galvanomagnetic effects in n-type bismuth telluride, *Proc. Phys. Soc.* 71, 430 (1958).
- [38] J. R. Drabble, Galvanomagnetic effects in p-type bismuth telluride, *Proc. Phys. Soc.* 72, 380 (1958).
- [39] P. A. Walker, The thermal conductivity and thermoelectric power of bismuth telluride at low temperatures, *Proc. Phys. Soc.* 76, 113 (1960).
- [40] H. J. Goldsmid, Heat conduction in bismuth telluride, *Proc. Phys. Soc.* 72, 17 (1958).
- [41] H. J. Goldsmid, The Ettingshausen figure of merit of bismuth and bismuth - antimony alloys, *Br. J. Appl. Phys.* 14, 271 (1963).
- [42] T. C. Harman and J. M. Honig, Theory of galvanothermomagnetic energy conversion devices. II. Refrigerators and heat pumps, *J. Appl. Phys.* 33, 3188 (1962).
- [43] M. Mizuguchi and S. Nakatsuji, Energy-harvesting materials based on the anomalous Nernst effect, *Sci. Technol. Adv. Mater.* 20, 262 (2019).
- [44] R. T. Delves, Thermomagnetic effects in semiconductors and semimetals, *Rep. Prog. Phys.* 28, 249 (1965).
- [45] J. S. Xiang, S. L. Hu, M. Lyu, W. L. Zhu, C. Y. Ma, Z. Y. Chen, F. Steglich, G. F. Chen,

and P. J. Sun, Large transverse thermoelectric figure of merit in a topological Dirac semimetal, *Sci. China: Phys., Mech. Astron.* 63, 237011 (2020).

[46] N. Roschewsky, E. S. Walker, P. Gowtham, S. Muschinske, F. Hellman, S. R. Bank, and S. Salahuddin, Spin-orbit torque and Nernst effect in Bi-Sb/Co heterostructures, *Phys. Rev. B* 99, 195103 (2019).

[47] A. Bose, A. S. Shukla, S. Dutta, S. Bhuktare, H. Singh, and A. A. Tulapurkar, Control of magnetization dynamics by spin-nernst torque, *Phys. Rev. B* 98, 184412 (2018).

[48] R. Mansfield and W. Williams, The electrical properties of bismuth telluride, *Proc. Phys. Soc.* 72, 733 (1958).

[49] C. Champness and A. Kipling, The nernst and magnetoresistance effects in nonstoichiometric bismuth telluride, *J. Phys. Chem. Solids* 27, 1409 (1966).

[50] M. K. Zhitinskaya, S. A. Némov, and T. E. Svechnikova, Effect of inhomogeneities of Bi<sub>2</sub>T<sub>3</sub> crystals on the transverse Nernst-Ettingshausen effect, *Semiconductors* 31, 375 (1997).

[51] G. Moreau, Sur les phénomènes thermomagnétiques, *Journal de Physique Théorique et Appliquée* 9, 497 (1900).

[52] P. Giannozzi, S. Baroni, N. Bonini, M. Calandra, R. Car, C. Cavazzoni, D. Ceresoli, G. L. Chiarotti, M. Cococcioni, I. Dabo, A. Dal Corso, S. De Gironcoli, S. Fabris, G. Fratesi, R. Gebauer, U. Gerstmann, C. Gougoussis, A. Kokalj, M. Lazzeri, L. Martin-Samos et al., Quantum espresso: A modular and open-source software project for quantum simulations of materials, *J. Phys.: Condens. Matter* 21, 395502 (2009).

[53] D. Vanderbilt, Soft self-consistent pseudopotentials in a generalized eigenvalue formalism, *Phys. Rev. B* 41, 7892 (1990).

[54] J. P. Perdew, K. Burke, and M. Ernzerhof, Generalized Gradient Approximation Made Simple, *Phys. Rev. Lett.* 77, 3865 (1996).

[55] G. K. Madsen and D. J. Singh, BoltzTraP. A code for calculating band-structure dependent quantities, *Comput. Phys. Commun.* 175, 67 (2006).

[56] T. Hirahara, T. Nagao, I. Matsuda, G. Bihlmayer, E. V. Chulkov, Y. M. Koroteev, P. M. Echenique, M. Saito, and S. Hasegawa, Role of Spin-Orbit Coupling and Hybridization Effects in the Electronic Structure of Ultrathin Bi Films, *Phys. Rev. Lett.* 97, 146803 (2006).

[57] K. Xiong, W. Wang, H. N. Alshareef, R. P. Gupta, J. B. White, B. E. Gnade, and K. Cho, Electronic structures and stability of Ni/Bi<sub>2</sub>Te<sub>3</sub> and Co/Bi<sub>2</sub>Te<sub>3</sub> interfaces, *J. Phys. D* 43, 115303 (2010).

[58] H. Zhang, X. Luo, C. Wang, Y. Xiong, S. Li, and X. Chen, Characterization of nanocrystalline bismuth telluride (Bi<sub>2</sub>Te<sub>3</sub>) synthesized by a hydrothermal method, *J. Cryst. Growth* 265, 558 (2004).

[59] S. Shigetomi and S. Mori, Electrical properties of Bi<sub>2</sub>Te<sub>3</sub>, *J. Phys. Soc. Jpn.* 11, 915

(1956).

[60] C. H. Champness and A. L. Kipling, The Hall and Seebeck effects in nonstoichiometric bismuth telluride, *Can. J. Phys.* 44, 769 (1966).

[61] J. P. Heremans, R. J. Cava, and N. Samarth, Tetradymites as thermoelectrics and topological insulators, *Nat. Rev. Mater.* 2, 17049 (2017).

[62] S. Cai, J. Guo, V. A. Sidorov, Y. Zhou, H. Wang, G. Lin, X. Li, Y. Li, K. Yang, A. Li, Q. Wu, J. Hu, S. K. Kushwaha, R. J. Cava, and L. Sun, Independence of topological surface state and bulk conductance in three-dimensional topological insulators, *npj Quantum Mater.*, 3, 62 (2018).

[63] J. Liang, L. Cheng, J. Zhang, H. Liu, and Z. Zhang, Maximizing the thermoelectric performance of topological insulator Bi<sub>2</sub>Te<sub>3</sub> films in the few-quintuple layer regime, *Nanoscale* 8, 8855 (2016).

[64] G. S. Nolas, J. Yang, and H. J. Goldsmid, Semiconductors and Thermoelectric Materials, in *Thermal Conductivity* (Springer, New York, 2006), pp. 123–152.

[65] See Supplemental Material at <http://link.aps.org/supplemental/10.1103/PhysRevMaterials.5.015403> for the temperature dependence of the thermoelectric and thermomagnetic figure of merit.

[66] K. Behnia, *Fundamentals of Thermoelectricity* (Oxford University Press, New York, 2015).

[67] A. C. Smith, J. F. Janak, and R. B. Adler, *Electronic Conduction in Solids*, Tech. Rep. (McGraw-Hill, New York, 1967).

[68] K. Behnia and H. Aubin, Nernst effect in metals and superconductors: a review of concepts and experiments, *Rep. Prog. Phys.* 79, 046502 (2016).